J. Fluid Mech. (1995), *vol.* 303, *pp.* 1–21

Effects of interaction between Marangoni and double-diffusive instabilities

By J. TANNY,† C. C. CHEN AND C. F. CHEN
Department of Aerospace and Mechanical Engineering, The University of Arizona, Tucson, AZ 85721, USA

(Received 15 August 1994 and in revised form 5 May 1995)

The effect of surface tension on the onset of convection in a horizontal double-diffusive layer was studied both experimentally and by linear stability analysis. The experiments were conducted in a rectangular tank with base dimension of 25 × 13 cm and 5 cm in height. A stable solute (NaCl) stratification was first established in the tank, and then a vertical temperature gradient was imposed. Vertical temperature and concentration profiles were measured using a thermocouple and a conductivity probe and the flow patterns were visualized by a schlieren system. Two types of experiments were carried out which illustrate the effect of surface tension on the onset of convection. In the rigid–rigid experiments, when the critical thermal Rayleigh number, R^T, is reached, large double-diffusive plumes were seen simultaneously to rise from the heated bottom and descend from the cooled top. In the rigid–free experiments, owing to surface-tension effects, the first instability onset was of the Marangoni type. Well-organized small plumes were seen to emerge and persist close to the top free surface at a relatively small R_M^T (where subscript M denotes 'Marangoni'). At larger $R_t^T > R_M^T$ (where subscript t denotes 'top') these plumes evolved into larger double-diffusive plumes. The onset of double-diffusive instability at the bottom region occurred at a still higher $R_b^T > R_t^T$ (where subscript b denotes 'bottom'). A series of stability experiments was conducted for a layer with an initial top concentration of 2 wt% and different concentration gradients. The stability map shows that in the rigid–free case the early Marangoni instability in the top region reduces significantly the critical R^T for the onset of double-diffusive convection. Compared with the rigid–rigid case, the critical R^T in the top region is reduced by about 60% and in the bottom region by about 30%. The results of the linear stability analysis, which takes into account both surface-tension and double-diffusive effects, are in general agreement with the experiments. The analysis is then applied to study the stability characteristics of such a layer as gravity is reduced to microgravity level. Results show that even at $10^{-4}g_0$, where g_0 is the gravity at sea level, the double-diffusive effect is of equal importance to the Marangoni effect.

1. Introduction

Under terrestrial gravity, convective motion driven by surface-tension gradients is noticeable only in very shallow (~ 1 mm thick) fluid layers. Otherwise, buoyancy effects are the dominant driving forces. However, when a thick fluid layer stably stratified by solute concentration is heated from below, it is likely that Marangoni convection will onset at the free surface while the bulk fluid is still stationary owing to stable density stratification. The interactions between the Marangoni and double-

† Permanent address: Center for Technological Education Holon, POB 305, Holon 58102, Israel.

diffusive instabilities as the gravity is reduced from the terrestrial to the microgravity level is a problem not only of theoretical interest, but of practical value. This latter aspect arises when manufacturing processes in which there are temperature and concentration gradients in a fluid layer with a free surface are carried out in space. Laboratory experiments to investigate such interactions can be readily carried out on Earth and, with some care, in space.

With this objective in mind, one of us (Chen 1991) conducted a series of experiments on a layer of stratified salt solution with a free surface heated from below. The stratification was obtained by filling the test tank with successive layers of constant-concentration salt solution. The top layer was always distilled water. The results were completely unexpected. The fluid motion at the onset of instabilities in a layer with a free surface was found to be no different than that in a layer with a rigid top boundary. Within experimental error, the critical thermal Rayleigh numbers for the two cases are the same. In order to gain some theoretical insight to the problem, a linear stability analysis for such a fluid layer was developed (Chen & Su 1992). Results indicate that the onset of instability should occur at a much lower thermal Rayleigh number when reasonable surface-tension gradients with respect to temperature and solute concentration are assumed. Since water is notorious for its susceptibility to surface contamination (see for example Platten & Villers 1988) the abnormal experimental results are thought to be the consequence of such contamination. The effect of surface contaminants in these experiments is to reduce the surface-tension gradients due to temperature and concentration to essentially zero.

Recently we carried out a series of experiments in which the initial salt concentration at the free surface was gradually increased from 0 wt% to 3 wt% in an effort to reduce the effect of surface contamination. In these experiments, a constant initial stratification was maintained. We found that contamination was indeed reduced as the initial concentration at the free surface was gradually increased from 0 wt% to 1.5 wt%. In the range of 1.5 wt% to 3 wt%, the onset of instabilities occurred at the same thermal Rayleigh number, and the convection pattern at onset, which is clearly of the Marangoni type, remained the same. Based on these results, we conducted experiments on fluid layers with increasing initial stable stratification and an initial salt concentration of 2 wt% at the free surface.

In this paper, we report the observed results of the interactions between the Marangoni and the double-diffusive instabilities. The experimental apparatus and procedure are described in §2. The results of the preliminary experiments and the interaction experiments are presented separately in §§3 and 4, respectively. In §5, the results of the linear stability analysis are compared to those obtained by experiment, with satisfactory agreement. Then, the analysis is applied to study the effect on the stability characteristics of the fluid layer of reducing gravity to a microgravity level. The results of our investigations are discussed in §6, and the major conclusions are presented in §7.

2. Experimental apparatus and procedures

2.1. *Apparatus*

The experiments were conducted in a rectangular box with inner base dimension of 25×13 cm and 5 cm high. The sidewalls of the box were made of optical glass to facilitate schlieren flow visualization (see below). The top and bottom constant-temperature plates were made of stainless steel but in most of the experiments with the free surface, a brass top plate was used. In both cases, the top plate, which was

removable, was provided with passages through which water from a constant-temperature bath could circulate. Beneath the bottom plate of the box was an aluminium base, in which water could circulate through passages. In order to ensure good thermal contact between the aluminium base and the stainless steel plate, a thermal joint compound was applied to all contact surfaces. Thermocouples were embedded in the top and bottom plates of the box near the inside surfaces. Their output was recorded and linearized using a Data Logger. The top and bottom of the box were insulated with 5 cm thick styrofoam. The sidewalls were not insulated to allow for continuous flow visualization during the experiment. This did not seem to influence the results because the temperature differences attained were usually small (not larger than 6 °C above or below room temperature). Water at different constant temperatures was supplied to each plate by two separate constant-temperature baths.

Vertical concentration and temperature profiles were measured by a dual probe consisting of a four-electrode Micro Scale Conductivity Instrument (MSCI, Precision Measurement Engineering, CA) and a thermocouple. The sensor of the MSCI and the thermocouple junction were located at the same vertical level, at a horizontal distance of 0.3 cm. The probe was traversed vertically through the stratified fluid at a constant speed of about 0.11 mm s^{-1}, recording the conductivity and temperature each 10 s, which resulted in about 40 data points over the layer depth. Data were always recorded while the probe was traversed downwards, with the two sensors ahead of the probe holder, to minimize any disturbances at the measured region. The MSCI was calibrated before and after each experiment against six solutions of known concentrations. The output voltage of the MSCI was translated into concentration using the local measured temperature and the relations for aqueous NaCl solution given by Head (1983).

The convective motions were visualized using the schlieren technique. The schlieren system consisted of two spherical mirrors, 15.24 cm in diameter and 152.4 cm in focal length, a white light source and a knife edge. The system was set up such that the circular parallel beam was passed horizontally through the mid-section of the tank visualizing an approximately 13 cm section out of the total box length of 25 cm. The output of the schlieren system was imaged by a CCD camera, and was displayed on a monitor and also recorded by a time-lapse VCR for later reviewing. The flow was also visualized by particles using a suspension of rheoscopic concentrate. The suspension was added to the stratified fluid in a uniform concentration of 0.15 wt %. The particles were used to visualize the structure of the flow from the top.

2.2. *Procedures*

In all experiments the depth of the salt-stratified fluid layer was 4 cm. In the experiments with a rigid surface (R–R), the top plate was put on Plexiglas supports of height 4 cm, such that the fluid was in contact with the plate. In the experiments with a free surface (R–F), Plexiglas supports 4.9 cm in height were used, thus forming an air gap of 9 mm thickness above the fluid surface. Many experiments on convection driven by surface-tension gradients were performed with a very narrow air gap between the liquid and the cooling plate (e.g. Koschmieder & Biggerstaff 1986). The analysis of Ferm & Wollkind (1982) suggests that a small air gap tends to enhance the stability of the layer. Furthermore, the large evaporation rates of the aqueous solutions used here preclude the use of small air gaps since condensation on the top plate substantially alters the gap shape and size during the experiment.

Before starting each experiment the box was filled with eight layers of salt solution of equal thickness (0.5 cm) but with decreasing concentration. The filled box was left to stand for 2 h. A one-dimensional time-dependent numerical calculation that we

developed predicted that the eight-layer structure would become smooth by molecular diffusion within this time period. This was verified by the concentration profile measured 2 h after filling the tank. During the 2 h waiting period, the stratified fluid was brought to an almost uniform temperature by applying equal temperatures at the top and bottom plates.

In the case of R–R boundaries, each experiment started by increasing the bottom plate temperature by 0.5 °C and decreasing the top plate temperature by 0.5 °C, thus imposing a temperature difference of 1 °C across the layer. This temperature change was allowed to diffuse across the layer over a period of 50 min, the heat diffusion time for a water layer 2 cm thick. Then an additional change of 1 °C was imposed across the layer, and so on. In the experiments with R–F boundaries the same procedure was employed except that the top plate temperature was reduced by 1.5 °C in each adjustment because of the air gap. The resulting actual change of the fluid surface temperature was later estimated by the measured vertical temperature profile. The vertical profiles of concentration and temperature were always measured before each temperature adjustment, when the system was in a quasi-steady state.

The temperature gradient was increased until double-diffusive instability plumes were observed at the bottom and top plates. In those experiments where instability started near one plate before the other, the temperature gradient was further increased until both the top and bottom regions became unstable. At this slightly supercritical condition, the system was allowed to stand for a few hours until a state of turbulent thermal convection across the layer was reached.

3. Preliminary experiments

The first experimental study on the effect of surface tension on double-diffusive instability was done by Chen (1991) in an experimental facility essentially similar to the present one. Chen heated from below stratified layers of different solutes, with the same density gradient. He established the concentration gradient by filling the box with four layers of solution, the top 1 cm layer was always pure water. In his R–F experiments, using the shadowgraph technique, the first instability onset was double-diffusive at the bottom region and later double-diffusive plumes appeared at the top region. Only very weak plumes were observed in the box corners before the onset of double-diffusive instability at the top, and these were attributed by Chen (1991) to surface-tension effects.

Our preliminary set of experiments was aimed at understanding what parameters control the surface-tension properties in our system. Since the surface-tension properties vary with the salt content of the top layer, we studied the effect of the top-layer concentration on the stability characteristics of the layer. We have carried out a series of experiments with R–F boundary conditions, with the same initial overall concentration difference $\Delta S^0 = 0.7$ wt%, but with different initial top-layer concentrations, in the range $0 \leqslant S_{top} \leqslant 3$ wt%. For each experiment we calculated the critical value of the thermal Rayleigh number, R^T, for the appearance of convective plumes in the fluid. This critical R^T (as defined in §4.2) was based on the measured linear vertical temperature profile.

The results are shown in figure 1, in which we now focus on the cross symbols which correspond to the first onset of instability at the top region, in the form of small plumes, later referred to as Marangoni instability (see §4.1). In the experiment with $S_{top} = 0$ wt% the Marangoni instability was not observed, in agreement with the observation by Chen (1991). However, as S_{top} was increased to 0.5 wt% the

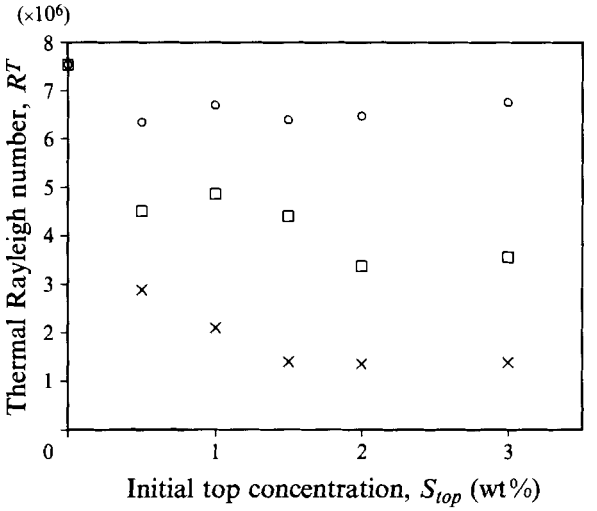

FIGURE 1. The effect of the initial top-layer concentration S_{top} on the critical R^T in the R–F case. The overall concentration difference $\Delta S^0 = 0.7$ wt%. ×, Marangoni instability; □, ○, double-diffusive instability in the top and bottom regions, respectively.

Marangoni instability appeared at relatively high R^T. As S_{top} was further increased, the critical R^T for the onset of Marangoni instability decreased, but for $S_{top} \geqslant 1.5$ wt% it seemed to approach a constant value. A similar trend is observed for the critical R^T for the onset of double-diffusive instability, marked in figure 1 by the open squares and circles.

These results imply that the surface properties change as S_{top} is increased from zero up to $S_{top} = 1.5$ wt% after which they apparently remain unchanged. We have chosen to study the stability of the layer in the range where the critical R^T for the onset of Marangoni and double-diffusive instabilities is essentially constant and, therefore, all the stability experiments were carried out with $S_{top} = 2.0$ wt%.

Another factor which can affect surface-tension phenomena is the cleanness of the surface. For example, Schwabe, Lamprecht & Scharmann (1988) have shown that a skin of dirt, formed on the fluid surface, can act like a solid layer, totally suppressing thermocapillary flow under microgravity conditions. In the context of gravity currents, Britter & Simpson (1978), Huppert & Simpson (1980), Didden & Maxworthy (1982) and Lister & Kerr (1988) noted that surface contamination caused the air–liquid interface to act as a rigid rather than a free surface. In the present study, the salt solutions were made of distilled water and analytical NaCl but otherwise no special precautions were taken to keep the test box and its environment clean. Therefore it was necessary to study the experimental repeatability by performing the same experiment several times. With respect to the onset of the Marangoni instability, very good repeatability was found within the error limits. This is shown in the stability map below (see figure 5).

4. Results

4.1. *Observations*

In this section we describe the sequences of events in two experiments with different boundary conditions. The initial overall salinity gradient was the same, with the bottom 0.5 cm layer at 2.7 wt% and the top layer at 2.0 wt%. Experiment 18 was

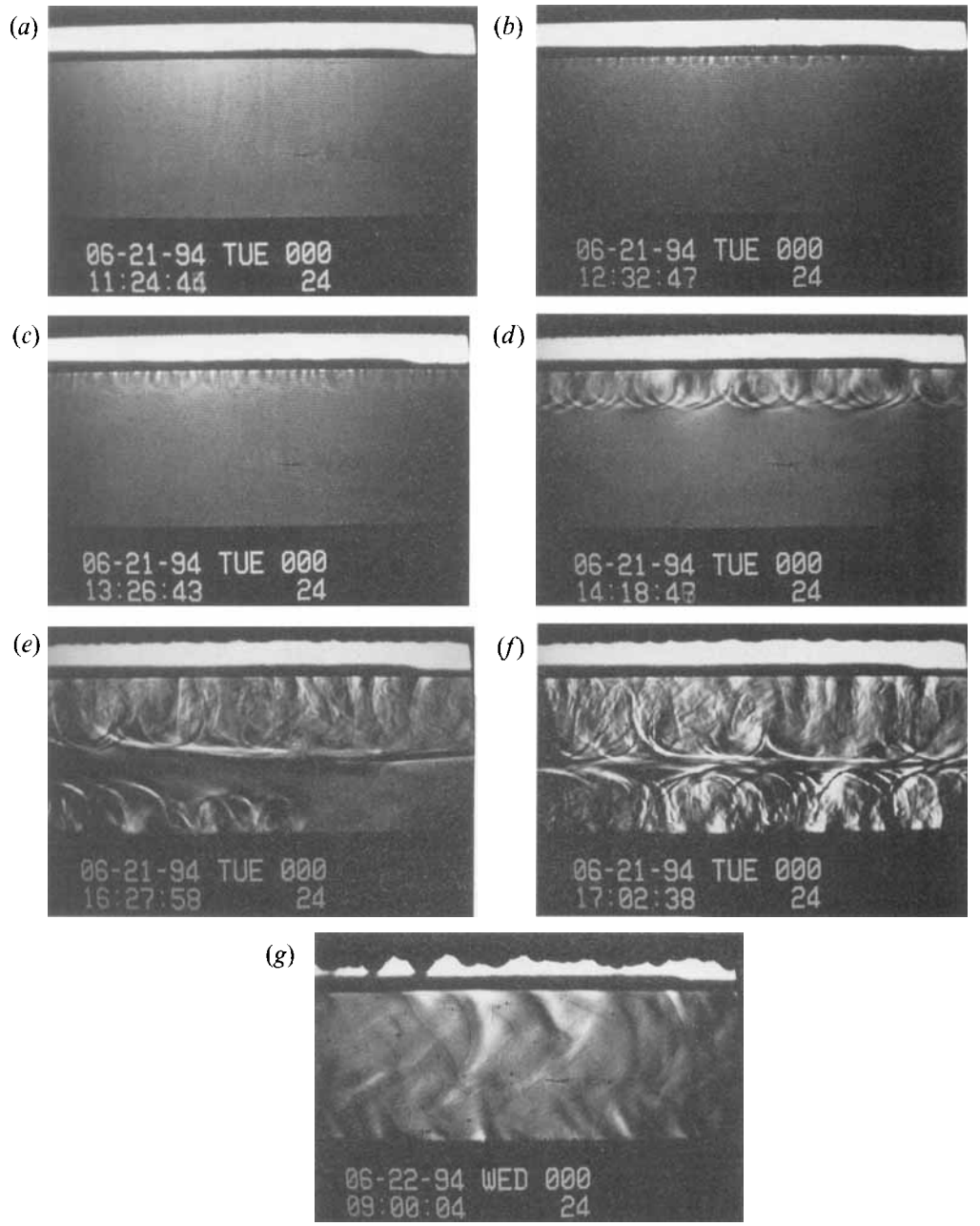

FIGURE 2. The different flow patterns as observed by the schlieren technique in an R–F experiment with $\Delta S^0 = 0.7$ wt %. (*a*) Stable fluid layer; (*b*) onset of Marangoni instability in the top layer; (*c*) appearance of deeper buoyancy-driven plumes in the top layer; (*d*) onset of double-diffusive instability in the top region; (*e*) onset of double-diffusive instability in the bottom region; (*f*) two-layer structure; (*g*) turbulent natural convection in the fluid.

carried out with rigid–rigid (R–R) conditions, and experiment 30 with rigid-free (R–F) conditions. The observations are based on the flow visualization and the measured vertical profiles. Schlieren pictures (made by photographing the video monitor) of the different flow patterns in an R–F experiment, performed with the same conditions as

experiment 30, are shown in figure 2. A series of six concentration profiles for experiments 18 and 30 are shown in figure 3 along with the corresponding temperature profiles for experiment 30. The temperature difference mentioned in this section corresponds to an equivalent ΔT across the fluid layer. Its calculation method is given in §4.2 in detail. This description illustrates qualitatively the effect of surface tension on the stability characteristics of a double-diffusive layer. The quantitative analysis will be given in the following sections.

We first observe the schlieren picture at $t = 120$ min after filling the box, figure 2(*a*). The grey region is the stratified layer and the white region above is the air gap. This schlieren picture shows a uniformly grey fluid, indicating a stagnant state. The concentration profiles of the fluid layers in the R–R (left) and R–F (middle) cases are shown in figure 3(*a*). The two profiles are essentially the same. The corresponding temperature profile for the R–F experiment in figure 3(*a*, right) shows that the fluid is isothermal.

After two temperature adjustments where $\Delta T = 1.1$ °C, we can observe in the schlieren picture (figure 2*b*) very small cells, more or less equally spaced along the free surface. These cells are identified with the onset of 'Marangoni' instability. The fluid layer is simultaneously exposed to buoyancy and surface-tension effects so this instability is not purely surface-tension driven. However, it is caused by the forces at the free surface (this instability mode does not exist when the top is rigid or at the bottom region) and therefore it is hereinafter referred to as Marangoni instability. The Marangoni convection is confined to the neighbourhood of the free surface because of the stable density gradient in the fluid layer below. As seen in figure 3(*b*), the concentration of the fluid in the R–F case became uniform within a layer of 0.4 cm thickness below the free surface due to the convective mixing. This thickness is in agreement with the depth of the cells observed in figure 2(*b*). The temperature profile for this stage is not affected, because of the relatively high thermal diffusivity.

As the temperature difference was increased to $\Delta T = 2.6$ °C, buoyancy-driven convection in the form of plumes started near the free surface where the stabilizing salinity gradient was weakened by the Marangoni convection. These plumes coexist with the Marangoni cells as seen by the schlieren picture in figure 2(*c*). These plumes penetrated much deeper into the stratified fluid, and the mixed layer extended down to approximately 0.8 cm (see figure 3*c*, middle, at $t = 320$). The corresponding temperature profile is still almost linear. The appearance of the buoyancy-driven plumes is a direct consequence of the earlier Marangoni instability. When the surface is rigid, or at the bottom region, the only instability mode observed is double-diffusive.

Only after one more adjustment, when $\Delta T = 3.3$ °C, did the double-diffusive mushroom-like plumes appear, which caused the Marangoni convection cells to vanish as seen in the schlieren picture (figure 2*d*). The domination of the double-diffusive convection over the Marangoni convection was identified with the onset of double-diffusive instability at the top region. The more vigorous double-diffusive convection caused the top mixed layer to deepen down to 1.2 cm (as indicated by the concentration profile at $t = 370$ min in figure 3*d*, middle) and also slightly affected the temperature profile (figure 3*d*, right).

After two more temperature adjustments ($\Delta T = 4.7$ °C) double-diffusive convection started at the bottom as seen in the schlieren picture in figure 2(*e*). Convection in the top layer is highly vigorous at this stage. The concentration and temperature profiles at $t = 470$ min (figure 3*e*) also indicate the onset of convection at the bottom layer in the R–F case.

Up to this stage, the fluid in the R–R experiment was stable, as indicated by the

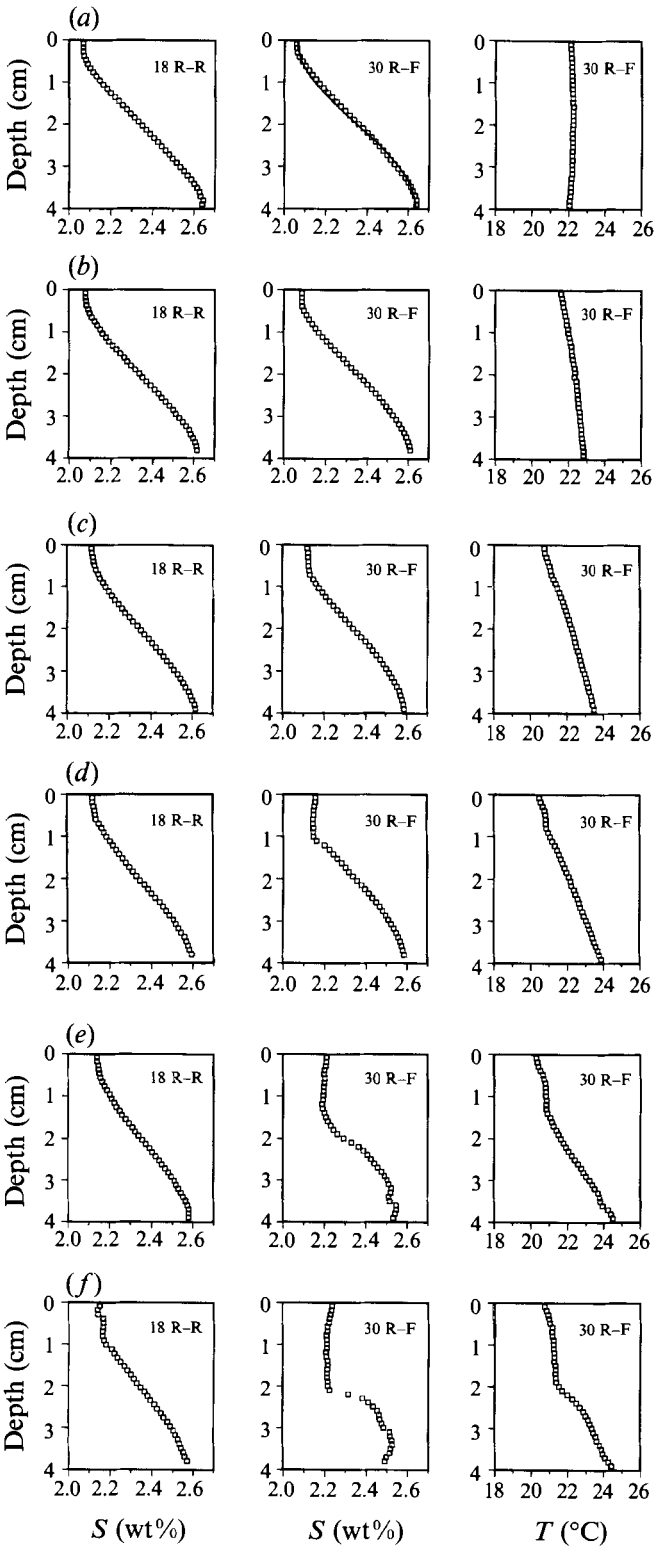

FIGURE 3. For caption see facing page.

diffusive concentration profiles in figure 3(*a–e*, left). At $t = 500$ min, double-diffusive convection occurred both at the top and the bottom plates in the R–R case, as indicated by the concentration profile in figure 3(*f*, left) ($\Delta T = 6.7$ °C). It is important to notice that in the R–R case the onset of convection did not always occur at the same temperature adjustment in the top and bottom regions (as in experiment 18 described here). In part of the experiments, the temperature difference between the top and bottom regions caused a considerable variation of the fluid properties, which in turn caused earlier onset of instability at the bottom, warmer, region. This will be further discussed below.

At that stage in the R–F case the convection in both top and bottom regions was well developed (figure 2*f*) but it is noticed that the upper region was much more mixed than the lower one (figure 3*f*, middle, $\Delta T = 5.3$ °C), because of the earlier instability at the top.

After the onset of double-diffusive convection in the top and bottom regions, the system was allowed to stand for a few hours. A state of turbulent natural thermal convection was eventually attained as seen in figure 2(*g*). The measured concentration and temperature profiles were essentially uniform.

The flow emerging at the onset of the Marangoni instability (figure 2*b*) was also observed from the top of the layer. The fluid was seeded with a suspension of a rheoscopic concentrate and the top layer was illuminated from the side by a horizontal light sheet. This was done in a different experiment with the same conditions as experiment 30. Immediately after the Marangoni cells were seen by the schlieren system the top plate of the box was removed for a short period of time (about 1 or 2 min), and the illuminated fluid was photographed. The observed flow pattern, as shown in figure 4, covers almost the whole free surface and seems to consist of a combination of cells and curved rolls. Bestehorn & Perez-Garcia (1987) performed a numerical simulation of Bénard–Marangoni instability in a fluid layer heated from below. It is remarkable that the structure observed in figure 4 is similar to some elements of the pattern obtained by Bestehorn & Perez-Garcia (see their figure 2).

The above visualization method was also used to observe the flow pattern at a later stage of the experiment when the double-diffusive plumes appeared. By moving the horizontal sheet of light to different levels within the fluid we could observe the structure of the double-diffusive plumes from the top. These observations were in agreement with the side view obtained by the schlieren technique, both indicating large mushroom-like plumes.

The double-diffusive plumes observed here (e.g. figure 2*d*) are similar to those observed by Shirtcliffe (1969) in his classical experiments on double-diffusive instability. He showed that the onset of instability in a stable stratified layer heated from below is oscillatory, as predicted by the linear theory (Turner 1973). Initially the oscillations were regular but with time their amplitude grew and they became disordered. When the oscillations became irregular, Shirtcliffe could observe mushroom-like plumes rising from the bottom of the tank, very similar to those observed here. Therefore, in the

FIGURE 3. Concentration and temperature profiles at different stages of experiment 30 (R–F) and experiment 18 (R–R). In both experiments $\Delta S^0 = 0.7$ wt%. (*a*) 120 min: the profiles at the stable isothermal state. The solid curve in the middle graph is the cosine fit to the measured concentration profile with $F = 0.82$ (see §5). (*b*) 220 min: onset of Marangoni instability in the R–F case. (*c*) 320 min: the appearance of deeper buoyancy-driven plumes in the top region in the R–F case. (*d*) 370 min: the onset of double-diffusive instability in the top region in the R–F case. (*e*) 470 min: the onset of double-diffusive instability in the bottom region in the R–F case. (*f*) 500 min: the onset of double-diffusive instability in the top and bottom regions in the R–R case and the two-layer structure in the R–F case.

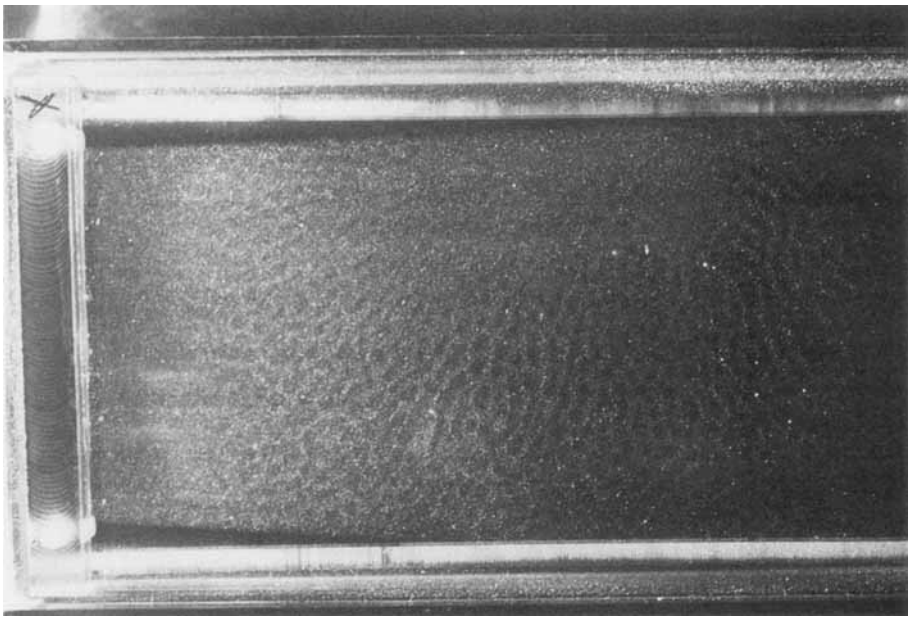

FIGURE 4. The structure of the flow immediately after the onset of the Marangoni instability as observed from the top.

present study, the appearance of such plumes was identified with the onset of double-diffusive instability.

One of the characteristics of double-diffusive convection is that instability can onset even when the density gradient is stabilizing (Turner 1973). In order to study whether the mushroom-like plumes observed in our experiments stem from double-diffusive processes we have calculated the local density gradient in the bottom region of the layer before the appearance of these plumes. We have chosen the bottom region because there we expect a pure double-diffusive instability without surface-tension effects. The calculation was done using the measured temperature and concentration profiles and the corresponding local values of α and β, the coefficients of thermal and solutal expansion that were calculated using the polynomials in Ruddick & Shirtcliffe (1979). In part of the experiments the calculated local density gradient was stabilizing throughout the bottom region, clearly indicating double-diffusive instability. However, in some experiments we found a destabilizing density gradient extending 2–4 mm from the bottom, into the fluid. This thickness is smaller than the thickness of the mushroom-like plumes in the bottom region, estimated to be about 10 mm in figure 2(*e*). Hence, in these latter cases the plumes onset in a layer which has both stabilizing and destabilizing local density gradients. Even in such a case the instability is dominated by double-diffusive processes.

4.2. *The governing parameters*

The dimensionless parameters governing this problem are the thermal and solute Rayleigh numbers, $R^T = g\alpha\Delta T h^3/\nu\kappa_t$ and $R_s = g\beta\Delta S h^3/\nu\kappa_t$, the Prandtl number $Pr = \nu/\kappa_t$ and the diffusivity ratio, $\tau = \kappa_s/\kappa_t$. Here g is the gravitational acceleration, α and β are the coefficients of thermal and solutal expansion, ΔT and ΔS are the temperature and concentration differences across the layer (as defined below), h is the layer thickness, ν is the kinematic viscosity, and κ_t and κ_s are the coefficients of thermal

and solutal diffusion respectively. The stability characteristics of the layer also depend on the thermal and solute Marangoni numbers, M_t and M_s, respectively, as defined below (equation (11)). However, the ratios R^T/M_t and R_s/M_s as defined in equation (13) depend only on the layer depth, gravity and some fluid properties. Since in our experiments the fluid properties do not change much these ratios are nearly constants (see table 2).

The top and bottom plates of the box are impermeable and therefore the concentration gradient established by the filling process described above is nonlinear and time-dependent (see figure 3(*a*). Therefore a proper definition of ΔS is needed. The experimental observations show that the onset of instability always occurs near the horizontal boundaries of the tank where the concentration gradient approaches zero. Therefore we have chosen an average constant gradient to represent the variable gradient across the layer. For this constant gradient we estimate ΔS as the instantaneous concentration difference between the fluid at the bottom and top plates. This ΔS and consequently R_s decrease with time owing to molecular solute diffusion.

In experiments with a free surface, the onset of Marangoni instability was usually earlier than the onset of double-diffusive instability. When the latter occurred, the concentration field was already disturbed by convection such that the concentration profile had a shape as shown, for example, in figure 3(*d*, middle). The top region is almost uniform, but near the bottom the diffusive profile is still valid. If at this state, ΔS is estimated as the concentration difference between the bottom and top (as defined above), it does not represent the concentration profile near the bottom in a manner which is consistent with the representation of the stable diffusive profile of figure 3(*a*, middle). Therefore at any time during the experiment, ΔS was estimated on the basis of the numerically calculated diffusive profile which corresponds to that time. In practice, the following procedure was implemented in all the experiments.

The concentration profile measured 2 h after filling the box was used to estimate an initial concentration difference, ΔS_0, which corresponds to time t_0. To estimate the critical ΔS_{cr} at an instability event occurring at time $t_{cr} > t_0$ during the experiment, the one-dimensional time-dependent numerical calculation of the evolution of the diffusive concentration profile in the box was used. This calculation started from the eight-layer structure, and was done with $\kappa_s = 1.45 \times 10^{-5}$ cm^2 s^{-1}.

First, the time at which the measured ΔS_0 is attained by the calculation was recorded. (This time was usually larger than 2 h because of the effect of mixing during the filling process. This effect decayed during the 2 h waiting period.) From that moment, the diffusive profile was allowed to evolve by diffusion for an additional time period of $t_{cr} - t_0$. The critical ΔS_{cr} is the one obtained after this period of time had elapsed. The ΔS calculated in this way was almost the same as the measured one, as long as the fluid was stable. Since the different instability events occur at different times, ΔS_{cr} and hence the critical R_s are different for each onset of instability in the same experiment.

For the estimation of the critical R^T the critical temperature difference ΔT_{cr} at each instability onset is needed. As in the case of the concentration profile, the temperature profile becomes distorted owing to the early instability at the top layer. Then the temperature profile is not linear any more, and the estimation of the critical temperature difference should be based on the temperature difference imposed between the plates. Just before each temperature adjustment, the temperature difference between the bottom and top plates, ΔT_s, was measured. For experiments with a rigid surface this temperature difference was identified with ΔT across the fluid layer. However, for the experiments with a free surface, the temperature drop across the air

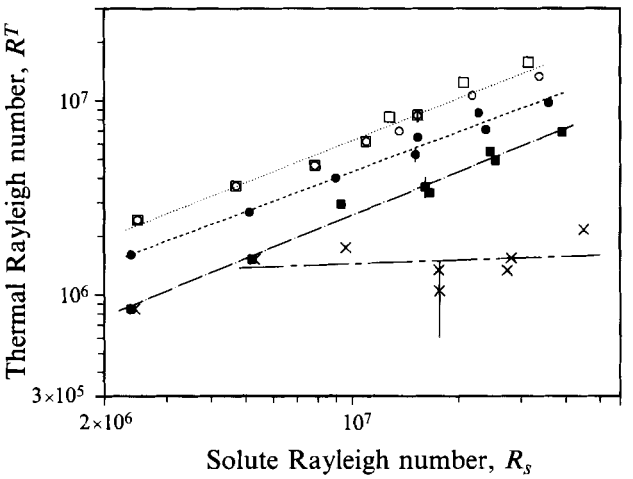

FIGURE 5. The stability map. ×, Marangoni instability; ■, ●, double-diffusive instability in the top and bottom regions, respectively, for the R–F case; □, ○, double-diffusive instability in the top and bottom regions, respectively, for the R–R case. The straight lines were fitted to the data points by the least-squares method. Vertical solid lines are error bars.

gap should be taken into account. For that purpose the measurements of the vertical temperature profile within the fluid were utilized. These measurements have shown that at the conduction state, where the profile is nearly linear, $\Delta T = C \times \Delta T_s$, where C is some coefficient. The value of C was found to vary between 0.3 and 0.5 and therefore its average value in each experiment was used to calculate ΔT across the fluid. The critical temperature difference was estimated as the average of the two ΔT values measured before and after an instability event. The error associated with ΔT_{cr} is not larger than ± 0.5 °C.

The physical properties of the fluid were estimated at the mean temperature and concentration in the layer at each instability onset. For these calculations we used the data given in Ruddick & Shirtcliffe (1979) Weast (1977), and Batchelor (1991).

4.3. *The stability map*

A total of sixteen experiments were conducted, eight with rigid–free conditions and eight with rigid–rigid conditions. The stability results are shown in figure 5 in which the critical thermal Rayleigh number is shown as a function of the solute Rayleigh number. The overall concentration difference ΔS^0 (i.e. the initial concentration difference between the top and bottom layers) was varied from 0.11 to 1.82 wt%. The initial R_s (at the onset of Marangoni instability in the R–F experiments) varied from 2.4×10^6 to 4.5×10^7. The physical conditions and the main results of the stability experiments are listed in table 1.

For the R–F cases, when $R_s > 5.3 \times 10^6$, the sequence of events is similar to what we described above and there are three distinct critical thermal Rayleigh numbers. R_M^T (denoted in figure 5 by crosses) represents the onset of the Marangoni instability, R_t^T (denoted by filled squares) is for the double-diffusive instability in the top region and R_b^T (denoted by filled circles) is for the double-diffusive instability at the bottom. But, for the two experiments with initial $R_s \leqslant 5.3 \times 10^6$, the onset of Marangoni and double-diffusive instability at the top occurred simultaneously (i.e. at the same temperature adjustment), such that $R_M^T = R_t^T$. This is because, at small R_s, the thickness of the top layer with a weak concentration gradient is increased and so is the size of the critical

Boundary conditions	ΔS^0	Marangoni instability			Double-diffusive top			Double-diffusive bottom		
		$R_s \times 10^{-6}$	ΔT_{cr} (°C)	$R^T \times 10^{-6}$	$R_s \times 10^{-6}$	ΔT_{cr} (°C)	$R^T \times 10^{-6}$	$R_s \times 10^{-6}$	ΔT_{cr} (°C)	$R^T \times 10^{-6}$
R–R	0.11	—	—	—	2.48	2.30	2.43	2.48	2.30	2.43
	0.21	—	—	—	4.70	3.19	3.64	4.70	3.19	3.64
	0.35	—	—	—	7.86	4.15	4.63	7.86	4.15	4.63
	0.49	—	—	—	10.96	5.06	6.16	10.96	5.06	6.16
	0.70	—	—	—	15.35	6.20	8.38	15.35	6.20	8.38
	0.70	—	—	—	12.81	8.41	8.21	13.60	7.02	6.96
	1.20	—	—	—	20.63	10.80	12.37	21.85	9.16	10.60
	1.82	—	—	—	31.50	13.53	15.83	33.80	11.26	13.36
R–F	0.11	2.44	0.93	0.85	2.38	0.93	0.85	2.38	1.73	1.60
	0.21	5.30	1.14	1.51	5.20	1.14	1.51	5.12	2.02	2.66
	0.35	9.60	1.19	1.74	9.32	1.98	2.93	8.98	2.74	3.99
	0.70	17.69	0.86	1.05	16.13	2.99	3.59	15.14	4.37	5.27
	0.70	17.60	1.09	1.34	16.61	2.70	3.36	15.35	5.12	6.45
	1.05	28.20	1.12	1.54	25.50	3.58	4.91	23.90	5.25	7.11
	1.20	27.50	1.13	1.33	24.64	4.61	5.48	22.84	7.14	8.64
	1.82	45.07	1.79	2.16	39.05	5.65	6.91	35.90	7.92	9.75

TABLE 1. Experimental conditions and results

Marangoni cells. When the size of these cells becomes comparable to the size of the plumes at the onset of double-diffusive instability, both modes can onset at the same R^T.

For the R–R case there is no Marangoni instability and so no R_M^T. For $R_s < 1.5 \times 10^7$, double-diffusive instability at the bottom (denoted by open circles) and at the top (denoted by open squares) occurred at the same R^T (with one exception) such that $R_t^T = R_b^T = R_r^T$ (where subscript r denotes 'rigid'). However, for $R_s > 1.5 \times 10^7$, the onset of double-diffusive instability at the bottom occurred at a smaller R^T than at the top because of the variable fluid properties (see §6).

Straight lines were fitted through the data points of figure 5 by the least-squares method. For the R–F case with $R_s > 5.3 \times 10^6$, R_M^T is nearly a horizontal line:

$$R_M^T = 5.05 \times 10^5 R_s^{0.065} \quad \text{when} \quad 5.3 \times 10^6 < R_s < 4.5 \times 10^7, \tag{1}$$

while R_t^T and $R_b^T \propto R_s^{0.75}$ and $R_s^{0.68}$, respectively:

$$R_t^T = 15.3 \times R_s^{0.75} \quad \text{when} \quad 2.4 \times 10^6 < R_s < 4.5 \times 10^7, \tag{2}$$

$$R_b^T = 70.63 \times R_s^{0.68} \quad \text{when} \quad 2.4 \times 10^6 < R_s < 4.5 \times 10^7. \tag{3}$$

For the R–R case and for $R_s > 1.5 \times 10^7$, the critical R^T for the onset of double-diffusive instability at the top and bottom is different. This is because of the temperature-dependent fluid properties as discussed below. However, the difference between the data points for the onset at the top and bottom is not large enough to distinguish a separate branch for each instability. Hence, a single straight line correlation yields

$$R_r^T = 56.36 \times R_s^{0.72}. \tag{4}$$

5. Linear stability analysis

Linear stability analysis of a double-diffusive fluid layer with surface-tension effects has been developed by Chen & Su (1992). In that analysis, the temperature and solute concentration distributions within the layer are assumed to be linear. In the experiments, the actual solute concentration distribution is nonlinear because both the top and bottom surfaces are impervious to mass transfer, see figure 3(*a*). The linear stability equations of Chen & Su are modified here to analyse the stability of a fluid layer with a nonlinear concentration profile. The theory will predict the critical condition for the onset of the first observed instability, the Marangoni instability.

The nonlinear concentration profile just prior to the onset of Marangoni instability can be represented quite accurately by a cosine profile. Murray & Chen (1989) found this to be true for a porous layer. The solute distribution is assumed to be

$$S = S_0 + F\frac{\Delta S}{2}\cos(\pi z/d), \quad 0 \leqslant z/d \leqslant 1, \tag{5}$$

where S_0 is the mean concentration of the layer, ΔS is the concentration difference across the layer determined by the methods stated in §4.2, and F is a constant factor chosen to fit the cosine profile to the actual one for each experiment. As shown in table 2 the range of F for all the R–F experiments is between 0.7 and 0.8, and for all the R–R experiments it is between 0.6 and 0.7. A typical cosine profile that was fitted to the data points with $F = 0.82$ is shown in figure 3(*a*, middle). As can be seen the agreement between the fitted profile and the measured one is very good.

Case	F	R_s	R^T	a	σ_i	R^T/M_t	R_s/M_s
R–R	0.74	2.54×10^6	2.293×10^6	11.7	884	—	—
	0.72	4.80×10^6	3.995×10^6	14.2	1125	—	—
	0.73	8.03×10^6	6.423×10^6	16.3	1427	—	—
	0.66	1.57×10^7	1.079×10^7	18.7	1843	—	—
	0.59	2.24×10^7	1.341×10^7	19.8	2054	—	—
	0.60	3.47×10^7	2.021×10^7	21.9	2510	—	—
R–F	0.77	2.490×10^6	1.323×10^5	15.5	323	18.5	−304.6
	0.76	5.400×10^6	2.512×10^5	18.7	484	25.6	−304.8
	0.80	9.802×10^6	3.512×10^5	22.0	692	27.3	−304.9
	0.79	1.808×10^7	3.909×10^5	25.8	981	23.6	−305.3
	0.74	2.815×10^7	4.377×10^5	28.5	1220	22.7	−305.8
	0.79	4.630×10^7	5.680×10^5	33.2	1721	23.0	−306.5

TABLE 2. Critical conditions as predicted by the linear stability theory

The linear stability equations for a basic solute distribution given by (5) become

$$\frac{1}{Pr}\frac{\partial}{\partial t'}(\mathrm{D}^2-a^2)\,W' = (\mathrm{D}^2-a^2)\,W' - a^2(R^T T' - R_s S'), \tag{6}$$

$$\frac{\partial T'}{\partial t'} = (\mathrm{D}^2-a^2)\,T' + W', \tag{7}$$

$$\frac{\partial S'}{\partial t'} = \tau(\mathrm{D}^2-a^2)\,S' + W'F\frac{\pi}{2}\sin(\pi z'), \tag{8}$$

in which W', T' and S' are the non-dimensional perturbation vertical velocity, temperature, and solute concentration, and t' and z' are the non-dimensional time and the vertical coordinate. The characteristic values corresponding to these variables are κ_t/d, ΔT, ΔS, d^2/κ_t and d, respectively. D denotes $\mathrm{d}/\mathrm{d}z'$ and a is the non-dimensional wavenumber. This set of equations is essentially the same as that given by Chen & Su (1992, equations 7–9) except for the multiplying factor $(\pi/2)F\sin(\pi z')$ of the last term in the solute conservation equation (8). The boundary conditions are

$$W' = \mathrm{D}W' = T' = \mathrm{D}S' = 0 \quad \text{at} \quad z' = 0, \tag{9}$$

$$W' = \mathrm{D}T' = \mathrm{D}S' = 0, \quad \mathrm{D}^2W' = -a^2(M_t T' + M_s S') \quad \text{at} \quad z' = 1, \tag{10}$$

in which the thermal and solutal Marangoni numbers are defined as

$$M_t = \frac{\gamma_t \Delta T d}{\rho\nu\kappa_t} \quad \text{and} \quad M_s = \frac{\gamma_s \Delta S d}{\rho\nu\kappa_t}, \tag{11}$$

where γ_t and γ_s are defined by equation (12) below. The bottom boundary is assumed to be rigid, non-diffusive, and at constant temperature. The top free surface is assumed to be plane and non-diffusive. The correct temperature condition is $\mathrm{D}T' = CT$(C is a constant). From Nield's (1964) results for the pure thermal case, we anticipate that the critical conditions will not be greatly altered if $\mathrm{D}T' = 0$. The last expression in (10) is the balance of the shear stress at the free surface due to viscosity and to the surface-tension gradient.

The surface tension σ of the fluid is assumed to be linearly dependent on both temperature and solute concentration:

$$\sigma = \sigma_0 - \gamma_t(T - T_0) - \gamma_s(S - S_0). \tag{12}$$

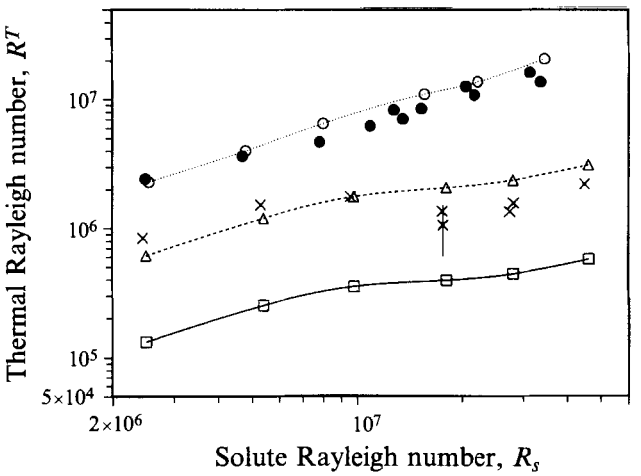

FIGURE 6. Critical thermal Rayleigh numbers as predicted by linear stability theory compared with the experimental values. Theoretical results for the R–R condition (· · · ○ · · ·); for the R–F condition with tabulated values of γ_t and γ_s (—□—); and for the R–F condition with reduced values of γ_t and γ_s (– – –△– – –); experimental results for the R–R condition (●); and R–F conditions (Marangoni instability) (×). The vertical solid line is an error bar.

It is to be noted that, for a given layer, the ratio of Rayleigh to Marangoni numbers is a constant:

$$\frac{R^T}{M_t} = \frac{\rho g \alpha d^2}{\gamma_t}; \quad \frac{R_s}{M_s} = \frac{\rho g \beta d^2}{\gamma_s}. \tag{13}$$

The eigenproblem defined by (6)–(8) and the related boundary conditions is solved by the Galerkin method using Chebyshev polynomials as the basis functions. We are indebted to Bruce Murray (1994, personal communication) for allowing us to use his computer code for the solution of this problem. Depending on the solute Rayleigh number and the boundary conditions, 48 or 64 terms are used in the expansions to effect convergence.

5.1. *Comparison with experimental results*

For each of the eight experiments conducted with a free surface, the ratios R^T/M_t and R_s/M_s are calculated using $\gamma_t = 0.157$ dyn cm^{-1} °C^{-1} for pure water and $\gamma_s = -0.367$ dyn cm^{-1} wt%$^{-1}$ for the salt solution (Weast 1977). We assume that the 2 wt% salt concentration has no effect on γ_t. With the experimental value of the solute Rayleigh number R_s as input, we determine the critical thermal Rayleigh number R^T, wavenumber a, and frequency of oscillations σ_i of the overstable instability mode at the marginal state. We first apply the theory to the R–R case in which Marangoni effects are absent. The critical thermal Rayleigh numbers are listed in table 2 and are also shown as a function of R_s in figure 6. The theoretical results are the open circles spline fitted with a dotted line, and the experimental results are the closed circles (cf. figure 5). It is seen that the agreement is excellent.

The results for the R–F case, also listed in table 2, are shown using open squares spline fitted with a full line in figure 6, and the experimental results are the crosses. It is seen that the predicted values have the same trend as the experimental results, though of lower magnitude. Note that the uncertainty in the experiments, shown as a straight line over the data at $R_s = 1.9\times10^7$, is comparable to the difference between the theoretical and experimental results. Our experiments have shown that, if, in the filling

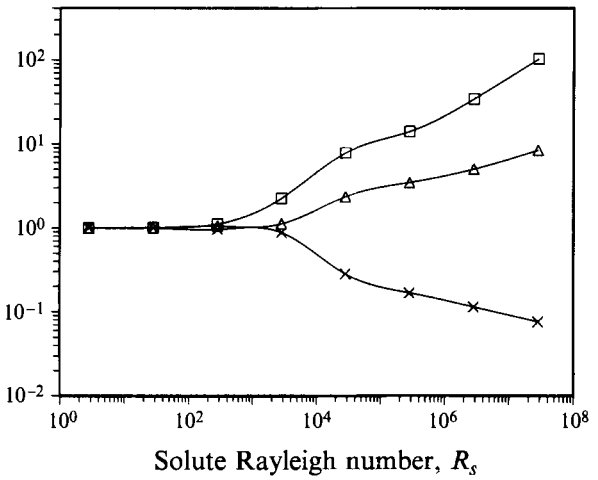

FIGURE 7. The effect of reduced gravity on the critical conditions. The critical thermal Marangoni number ratio, M_t/M_{t0} (—□—); the critical wavelength ratio, λ/λ_0 (—×—); and the critical oscillation frequency ratio (—△—).

process, the top layer consists of distilled water, the surface tension effects are essentially non-existent, or $\gamma_t = \gamma_s = 0$, at the onset of double-diffusive instability. It is, therefore, reasonable to expect that if, in the filling process, the top layer consists of a 2 wt% salt solution the actual values of γ_t and γ_s will be lower than those given by Weast (1977). We found by trial and error that when both γ_t and γ_s are reduced by a factor of 0.202, the predicted critical R^T agrees with the experimental value at $R_s = 9.802 \times 10^6$. Using the same factor in the other five cases, we obtain a theoretical curve, shown by the dashed line connecting the open triangles, which is in reasonable agreement with the experimental points. The theory also predicts increasing wavenumber with increasing R_s, again in agreement with the experimental observations. These results indicate that the linear stability theory correctly accounts for the competing effects of Marangoni and double-diffusive instabilities.

5.2. *Microgravity conditions*

We now examine the effect of reduced gravity on the onset of instabilities in a double-diffusive layer with a free surface by the use of the linear stability theory. We choose the case $R_s = 2.815 \times 10^7$ and $M_s = -9.205 \times 10^4$ and determine the critical conditions for instability as the gravity is reduced from g_0, gravity at sea level. At zero gravity, the critical thermal Marangoni number is $M_t = 186.3$, reflecting the rather weak stabilizing forces of the solutal Marangoni effect due to the cosine concentration distribution near the free surface. The critical wavenumber $a = 2.2$, and the frequency of oscillations $\sigma_i = 144.2$. The critical conditions have been determined for the range $R_s = 2.815$ to 2.815×10^7, while M_s is kept constant. The results in terms of M_t/M_{t0}, λ/λ_0 and σ_i/σ_{i0}, in which the subscript zero refers to the values at zero gravity and λ is the critical wavelength, are shown as a function of R_s in figure 7. The upper curve is for M_t/M_{t0}, which is essentially the ratio of the critical ΔT across the layer to that at zero gravity. It shows that even at $10^{-4}g_0$ ($R_s = 2.815 \times 10^3$), the critical ΔT is twice that at zero gravity owing to the buoyancy effect. As gravity (or R_s) is increased, the critical thermal Marangoni number and frequency of oscillation become large, while the critical wavelength becomes smaller, signifying the increasing importance of the buoyancy effect.

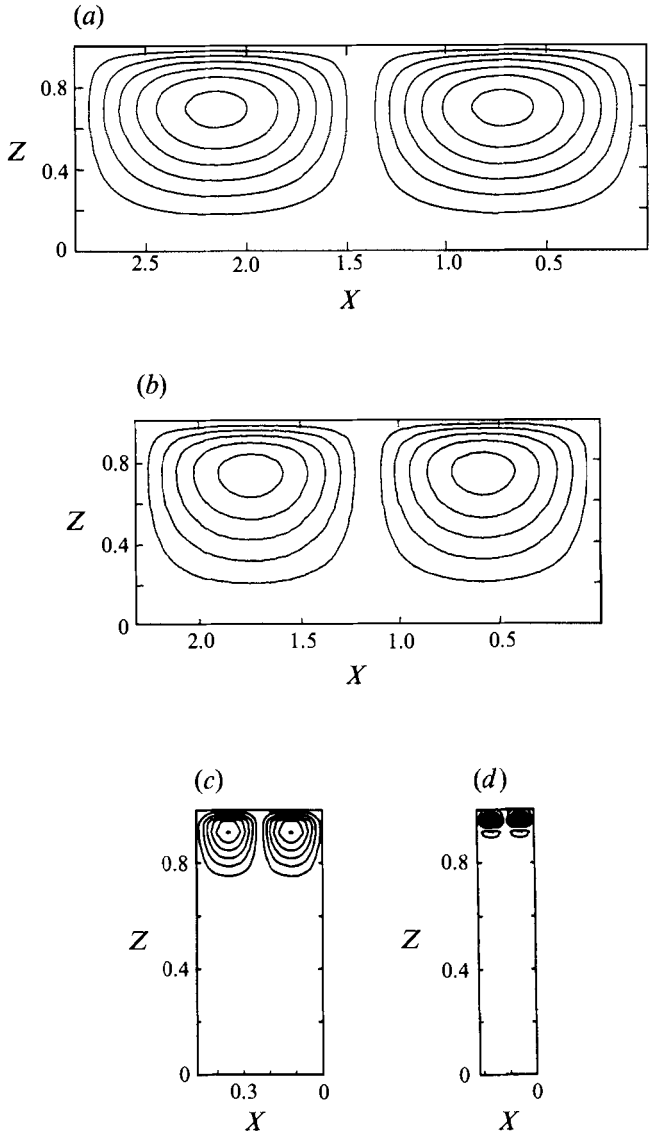

FIGURE 8. The effect of reduced gravity on the perturbation streamlines at the marginal state for the R–F case: (*a*) $R_s = 2.815$; (*b*) $R_s = 2.815 \times 10^3$; (*c*) $R_s = 2.815 \times 10^5$; (*d*) $R_s = 2.815 \times 10^7$ (at sea-level gravity).

Streamlines constructed from the eigenvector W' are obtained for $R_s = 2.815 \times 10^0$, $\times 10^3$, $\times 10^5$, and $\times 10^7$ and are shown in figure 8. The horizontal extent of each plot is the non-dimensional wavelength. The nearly square cells due to the Marangoni effect alone at $R_s = 2.815$ (at $10^{-7} g_0$) are gradually squeezed to the top of the layer as gravity is increased. At $R_s = 2.815 \times 10^7 (1 g_0)$, for a layer thickness of 4 cm, each cell would be approximately 0.5 cm wide and 0.3 cm deep. These dimensions are approximately equal to the observed ones.

6. Discussion

The main objective of this study is the effect of the Marangoni instability on the onset of double-diffusive convection. This effect is best illustrated by comparing the double-diffusive instability results in the R–F and the R–R cases. In figure 9 we plot the ratios R_t^T/R_r^T and R_b^T/R_r^T as a function of R_s using the straight lines fitted to each instability mode (equations (2), (3), (4)).

We observe that the two lines are nearly horizontal, indicating a weak dependence of the ratios on R_s. This is also indicated by the almost parallel lines on the stability map (figure 5). Since both ratios are smaller than unity, we conclude that the Marangoni instability reduces the critical R^T for the onset of double-diffusive convection as compared to the R–R case. In particular, $R_t^T/R_r^T \approx 0.42$ and $R_b^T/R_r^T \approx 0.7$.

The effect of the Marangoni instability is larger in the top than in the bottom region. In the top region the early Marangoni convection weakens the concentration gradient, as observed in the concentration profile of figure 3(*b*, middle). Consequently, double-diffusive instability will onset at a lower R^T than for an undisturbed concentration gradient, as seen in figure 3(*b*, left) for the R–R case. Hence, in the top region, subcritical double-diffusive instability is triggered by Marangoni instability.

In the bottom region double-diffusive instability occurs at a critical R^T which is lower by about 30% than its corresponding value for the R–R case. This phenomenon is mainly attributed to the existence of finite-amplitude disturbances in the fluid, which trigger a subcritical double-diffusive instability in the bottom region. The capability of finite-amplitude disturbances to trigger subcritical double-diffusive instability was also noted by Shirtcliffe (1969). Also, the convection in the top region can trigger double-diffusive instability in the bottom region indirectly through its effect on the profiles of concentration and temperature.

The line fitted to the data points of Marangoni instability in figure 5 is almost horizontal, i.e. R_M^T depends very weakly on R_s. This suggests that the Marangoni instability observed here is mainly caused by the gradient of the surface tension with temperature. The concentration gradient seems to have a very small effect on this instability mode. This phenomenon can be explained by the fact that before the onset of Marangoni instability, at the top of the layer, the temperature profile is linear but the concentration profile approaches zero because of the impermeable free surface (see figure 3*a*, middle and 3*b*, right). Thus the concentration gradient and hence R_s have a very small effect on the Marangoni instability.

Another interesting phenomena observed in the R–R experiments is the effect of the variable properties. It was mentioned before that in the R–R experiments with $R_s > 1.5 \times 10^7$ double-diffusive convection did not start simultaneously in the top and the bottom regions. The cause for this phenomenon is the temperature-dependent fluid properties, mainly the kinematic viscosity and the coefficient of thermal expansion. In the bottom region, the temperature was higher such that the viscosity was lower and the coefficient of thermal expansion was higher. In experiments with a large concentration difference ($R_s > 1.5 \times 10^7$) the critical temperature difference was large and so was the variation of the fluid properties. Therefore in such experiments, convection started first at the bottom, at a smaller critical temperature difference than that required to destabilize the top region. In low-concentration-gradient ($R_s < 1.5 \times 10^7$) experiments, the convection started simultaneously (i.e. within the same temperature adjustment) in the top and bottom regions. It is noticed that the same property variation existed in the R–F experiments. However, the effect of the

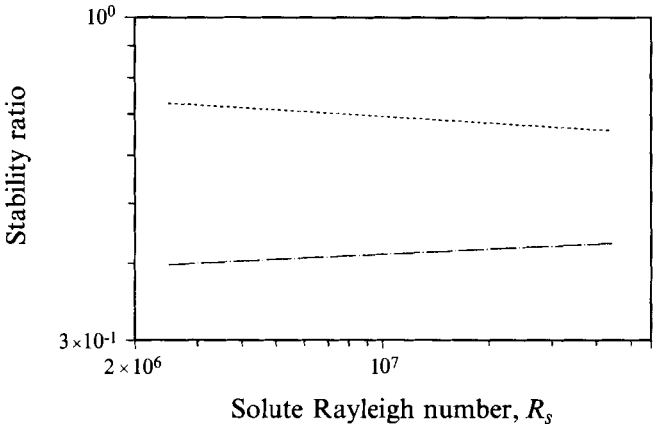

FIGURE 9. The stability ratio as a function of R_s. Chain-dashed line is R_t^T/R_r^T. Dashed line is R_b^T/R_r^T.

Marangoni instability at the top region overwhelmed the property variation such that in all the R–F experiments $R_t^T < R_b^T$.

The linear stability theory as developed by Chen & Su (1992) using Chebyshev polynomials as basis functions has been applied to predict the onset conditions of instabilities in the laboratory experiments with both rigid–rigid and rigid–free boundary conditions. The onset of double-diffusive instability in a layer with R–R conditions using the realistic (cosine) salinity distributions shows remarkable agreement with the experimental data, even though the experimental Rayleigh numbers are very large, 10^6–10^7. For the R–F case, good agreement can be obtained when both γ_t and γ_s are reduced from their accepted values owing to the presence of impurities on the surface. After validation by the experimental results, linear stability theory was applied to study the effect of microgravity on the onset of instabilities. It is found that, as the gravity is reduced, the critical Marangoni number is likewise reduced and the critical wavelength is increased. The buoyancy effect remains noticeable even at $10^{-4}g_0$; the critical ΔT for the onset of instabilities is approximately twice that at zero gravity.

7. Conclusions

The following conclusions can be reached from the results of the experiments and the linear stability analysis.

(i) For a double-diffusive layer with a free surface, at high initial solute Rayleigh numbers ($R_s > 5.3 \times 10^6$), the first instability to occur is the Marangoni instability at the free surface. At successively higher thermal Rayleigh numbers, double-diffusive instability first appears at the free surface, then at the bottom rigid surface.

(ii) At lower solute Rayleigh numbers ($R_s \leqslant 5.3 \times 10^6$), Marangoni and double-diffusive instabilities occur simultaneously at the free surface. Double-diffusive instability appears at the bottom rigid boundary at a higher thermal Rayleigh number.

(iii) The Marangoni convection at the free surface contributes substantially to the reduction in the critical thermal Rayleigh number for the onset of double-diffusive convection, compared to its values in the rigid–rigid case. In the top region, R^T is reduced by about 60% and in the bottom region by about 30%.

(iv) The linear stability analysis with an initial cosine salinity distribution yields results in reasonable agreement with the experimental results.

(v) For gravity as low as $10^{-4}g_0$ the double-diffusive effect is of equal importance as the Marangoni effect in destabilizing the fluid layer.

The authors gratefully acknowledge the financial support provided by NASA MSAD through grant NAG3-1386. The authors thank Mr Eric Zuercher for his assistance with the experiments and data reduction.

REFERENCES

BATCHELOR, G. K. 1991 *An Introduction to Fluid Dynamics*. Cambridge University Press.

BÉSTEHORN, M. & PEREZ-GARCIA, C. 1987 Coexistence of patterns with different symmetries in Bénard-Marangoni convection. *Europhys. Lett.* **4**, 1365–1370.

BRITTER, R. E. & SIMPSON, J. E. 1978 Experiments on the dynamics of a gravity current head. *J. Fluid Mech.* **88**, 223–240.

CHEN, C. F. 1991 Surface tension effects on the onset of double-diffusive convection. *Microgravity Sci. Tech.* **4**, 108–109. (Full paper appeared in *Microgravity Fluid Mechanics* (ed. H. J. Rath), pp. 325–333, Springer, 1992.)

CHEN, C. F. & SU, T. F. 1992 Effect of surface tension on the onset of convection in a double-diffusive layer. *Phys. Fluids* A **4**, 2360–2367.

DIDDEN, N. & MAXWORTHY, T. 1982 The viscous spreading of plane and axisymmetric gravity currents. *J. Fluid Mech.* **121**, 27–42.

FERM, E. N. & WOLLKIND, D. J. 1982 Onset of Rayleigh-Bénard-Marangoni instability: Comparison between theory and experiment. *J. Non-Equilib. Thermodyn.* **7**, 169–190.

HEAD, M. J. 1983 The use of miniature four-electrode conductivity probes for high resolution measurement of turbulent density or temperature variations in salt-stratified water flows. PhD thesis, University of California, San Diego.

HUPPERT, H. E. & SIMPSON, J. E. 1980 The slumping of gravity currents. *J. Fluid Mech.* **99**, 785–799.

KOSCHMIEDER, E. L. & BIGGERSTAFF, M. I. 1986 Onset of surface-tension-driven Bénard convection. *J. Fluid Mech.* **167**, 49–64.

LISTER, J. R. & KERR, R. C. 1989 The propagation of two-dimensional and axisymmetric viscous gravity currents at a fluid interface. *J. Fluid Mech.* **203**, 215–249.

MURRAY, B. T. & CHEN, C. F. 1989 Double-diffusive convection in a porous medium. *J. Fluid Mech.* **201**, 147–166.

NIELD, D. A. 1964 Surface tension and buoyancy effects in cellular convection. *J. Fluid Mech.* **19**, 341–352.

PLATTEN, J. K. & VILLERS, D. 1988 On thermocapillary flows in containers with differentially heated side walls. In *Physicochemical Hydrodynamics – Interfacial Phenomena* (ed. M. G. Velarde), pp. 311–336. Plenum.

RUDDICK, B. R. & SHIRTCLIFFE, T. G. L. 1979 Data for double diffusers: Physical properties of aqueous salt-sugar solutions. *Deep-Sea Res.* **26A**, 775–787.

SCHWABE, D., LAMPRECHT, R. & SCHARMANN, A. 1988 Experiments on steady and oscillatory thermocapillary convection in space with application to crystal growth. In *Physicochemical Hydrodynamics – Interfacial Phenomena* (ed. M. G. Velarde), pp. 291–310. Plenum.

SHIRTCLIFFE, T. G. L. 1969 An experimental investigation of thermosolutal convection at marginal stability. *J. Fluid Mech.* **35**, 677–688.

TURNER, J. S. 1973 *Buoyancy Effects in Fluids*. Cambridge University Press.

WEAST, R. C. 1977 *Handbook of Chemistry and Physics*. Cleveland: CRC Press.